International Journal of Microwave and Wireless Technologies

cambridge.org/mrf

Design of reconfigurable frequency selective surface for low-frequency band applications

Ashish Suri and Kumud Ranjan Jha

School of Electronics and Communication Engineering, Shri Mata Vaishno Devi University, Katra, India

Research Paper

Cite this article: Suri A, Jha KR (2025) Design of reconfigurable frequency selective surface for low-frequency band applications. *International Journal of Microwave and Wireless Technologies* **17**(10), 1794–1805. https://doi.org/10.1017/S1759078725102675

Received: 11 June 2025
Revised: 18 November 2025
Accepted: 3 December 2025

Keywords:
AFSS; high tuning ratio; metasurface; reconfigurable; stealth technology

Corresponding author: Ashish Suri;
Email: ashish.suri@smvdu.ac.in

Abstract

In this paper, a dual concentric square-loop dual-polarized reconfigurable frequency selective surface with a high tuning ratio of 2.02 operating in the 1.53–3.10 GHz band is proposed. This high tuning ratio has been achieved by using four SMV1430-LF varactor diodes, which have been actuated using a simple biasing arrangement made of stubs and four metallic vias per unit-cell. The unit-cell has been rigorously analyzed, and an equivalent circuit (EC) model has been developed for the physical insight. The proposed EC model also demonstrates the reconfigurability of the unit-cell and thus predicts its behavior. The effect of the angular incidence of the impinging electromagnetic wave on the structure up to a 45° has been experimentally verified, which demonstrates its angular stability and polarization insensitive behavior. The structure may find applications in the electromagnetic spectrum's *L, S*, and 2.45 GHz ISM bands.

Introduction

As more and more devices today use wireless connections, the demand for fast and reliable communication has grown quickly. The rapid evolution of modern communication systems, including the expansion of wireless networks, the infrastructures of internet of things, and defense-related technologies, has driven the demand for reconfigurable frequency selective surface (FSS) designs [1–3]. By integrating active components such as varactor diodes, positive-intrinsic-negative (PIN) diodes, or other tunable elements, it becomes possible to dynamically modify the frequency response, bandwidth, and even the polarization characteristics of the FSS [4–8]. This adaptability is particularly essential in environments where operating conditions depend on the dynamic availability of the electromagnetic spectrum for the intended applications, interference conditions, or the environment-based specific limitations.

While significant progress has been made in the development of reconfigurable FSSs for microwave and millimeter-wave bands, comparatively fewer studies have addressed the low-frequency band implementations. At lower frequencies, unit-cell dimensions tend to increase, presenting challenges for compactness, integration, and angular stability [9, 10]. Moreover, low-frequency FSS applications such as for the *L*/*S* band communication systems, low-frequency radar, and shielding effectiveness often require wide frequency tuning ranges without compromising the transmission characteristics in the intended band, which becomes a challenge to achieve [11–13].

The AFSS structures are made of self-repeating periodic elements with properties that allow them to control the transmission or reflection of electromagnetic (EM) waves. The selection of an element design determines the behavior and performance of FSS filters, which can also control the radiating behavior of the antennas when used as a superstrate. When PIN or the varactor diodes are embodied in this FSS superstrate, AFSS can electronically switch the antenna beam to make the structure suitable for the beam steering applications without the need for any external phase shifters. Switching ON and OFF the PIN diodes integrated FSS has been used to change the radiation pattern of the antennas to cover the entire azimuth plane [14–17]. However, by employing some innovative methods, the number of required elements can be drastically reduced, and ultimately, the design complexity of the beam-switching antenna can be reduced [18].

Varactor-based active frequency selective surfaces (AFSS) are an innovative concept that can also solve many problems in the beam-switching of antennas. This type of reconfigurable FSS uses the inherent advantages of varactor diodes, tunable semiconductor devices that allow real-time adaptability and precise frequency control [19, 20]. Integration of the varactor diodes in the FSS structure provides a revolutionary way to dynamically control the EM wave impinging on it, making it an essential technology for future-generation communication systems [21]. The main idea behind using the varactor-based active FSS is its capability to continuously switch between the reflective and transmissive states through electronic capacitance adjustment in the diodes integrated within the surface. Coupled with varactor diodes, the frequency response of an AFSS can be tuned to help antennas to reconfigure their beam positions [22–24].

© The Author(s), 2026. Published by Cambridge University Press in association with The European Microwave Association.

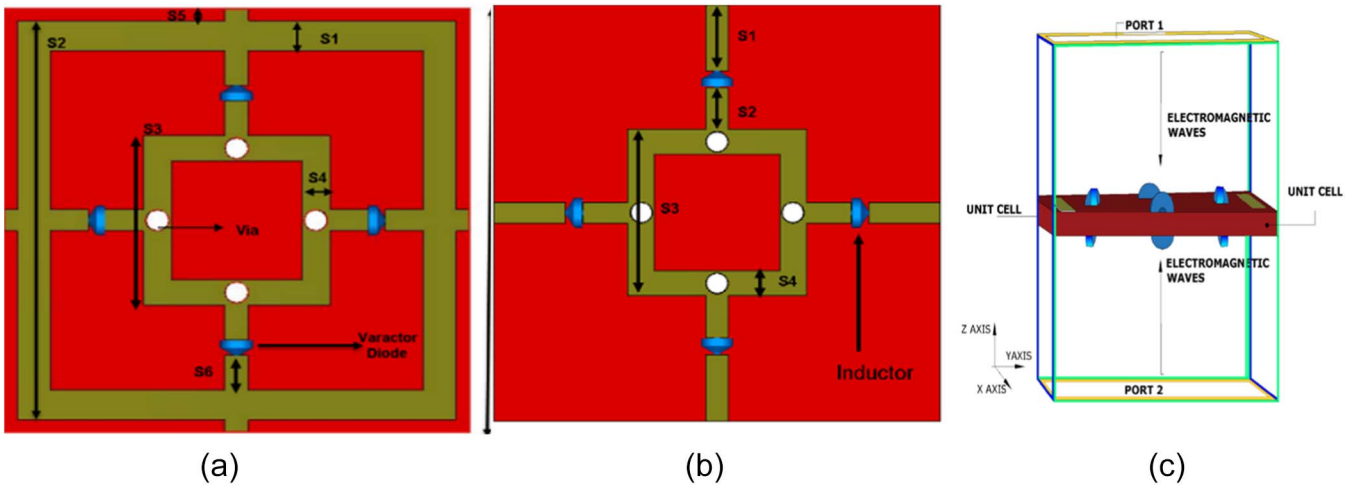


Figure 1. Proposed AFSS unit-cell (a) front, (b) back view, and (c) 3D view.

The varactor diode-based AFSS provides numerous advantages that make it better suited to overcome the beam-switching problems. It achieves compactness as it integrates varactor diodes in the FSS structure, thus removing the bulkier external components and setting it up for streamlined implementations even in space-constrained applications [25–27]. This integration also supports low power consumption since it requires minimal power for operation and thus makes it suitable for energy-consumption-based communication systems [28, 29]. A compensation mechanism based on a reconfigurable FSS with angular stability to compensate for the deviation introduced by the varactor diode is proposed in [30]. The PIN diode-operated dual-polarized tunable FSS working in the LTE-D band is reported in [31]. A tunable FSS with wide reconfigurability between 1.51 and 3.84 GHz, which has been achieved using varactor and PIN diodes simultaneously, is reported in [32]. Although the structure exhibits angular stability up to 70°, it is a single polarization structure, which may find limited applications. To realize high transmittance, a varactor-tunable FSS based on the equivalent circuit model (ECM) is proposed in [33]. Further, in the case of varactors, the frequency tuning is done with high precision because of high sensitivity and tunability. This results in greater adaptability of the AFSS under varying operating conditions, which makes it suitable for the beam steering applications. These benefits bring powerful capabilities to varactor-based active FSS reconfigurable antennas, which motivates researchers to implement innovative methods in designing and fabrication of this type of AFSS.

This paper advances reconfigurable FSS technologies by introducing a simple varactor-based AFSS design operating in the electromagnetic spectrum's *L, S*, and ISM bands. The key contributions include the development of optimized AFSS design principles and integrating varactor diodes for precise real-time frequency tuning, which may be used for dynamic beam-switching without the need for external phase-shifting components to reduce structural complexity. The paper comprehensively analyzes reconfigurable FSS for TE/TM modes with angular stability. The equivalent circuit (EC) model has been developed to demonstrate the congruence of the theoretical and structural responses. The paper addresses the challenges in designing the reconfigurable FSS. It thus proposes a simple reconfigurable FSS that can be tuned in the 1.53–3.1 GHz communication band with a high tuning ratio.

Table 1. Design parameters of unit-cell

Parameter	Value (mm)	Parameter	Value (mm)
Front view		*Back view*	
S_1	1.40	S_1	3.00
S_2	18.80	S_2	2.00
S_3	8.00	S_3	8.00
S_4	1.20	S_4	1.20
S_5	0.60	Via	0.5
S_6	1.65	Slots	0.5

The paper is organized as follows. Section "Proposed AFSS unit-cell" presents the proposed AFSS unit-cell design. In Section "Equivalent circuit model", the EC model of the reconfigurable AFSS, which shows tunability, is developed. Section "Theoretical validation" presents theoretical validation. Section "Fabrication and experimental results" presents the fabricated and experimental results. In Section "State-of-the-art comparison", the state-of-the-art comparison is made. Finally, Section "Conclusion" concludes the work.

Proposed AFSS unit-cell

The geometric structure of the unit-cell of the proposed AFSS is shown in Fig. 1(a) and (b). The unit-cell consists of two metallic surfaces placed at opposite faces of a dielectric. The upper metallic surface has a double square loop with stubs, while the bottom layer is a single square loop with stubs. These square loops in the unit-cell are responsible for the bandpass behavior of the AFSS. The RT-Duroid 5880 ($\varepsilon_r = 2.2$, $\tan\delta = 0.0008$) with a thickness (h) = 1.6 mm has been used as the substrate material. The capacitive gap between two square loops on the upper layer is connected through a varactor diode to obtain the frequency tuning. The proposed structure's upper layer has an outer square loop of 18.80 and 1.40 mm, while the inner square loop has an 8.00 mm length and 1.20 mm width, respectively. The structure's bottom layer comprises a single square loop 8.00 mm in length and 1.20 mm in width with stubs.

https://doi.org/10.1017/S1759078725102675 Published online by Cambridge University Press

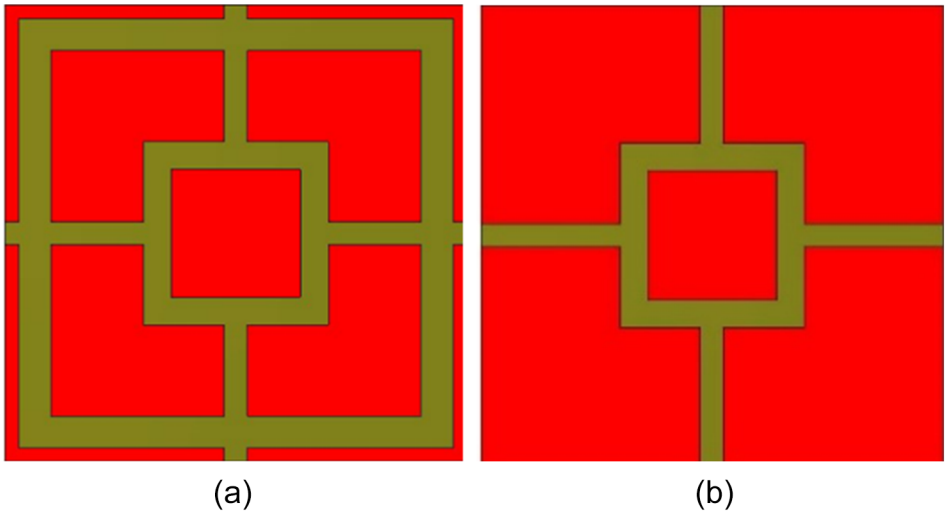


Figure 2. Proposed unit-cell (a) front and (b) back view.

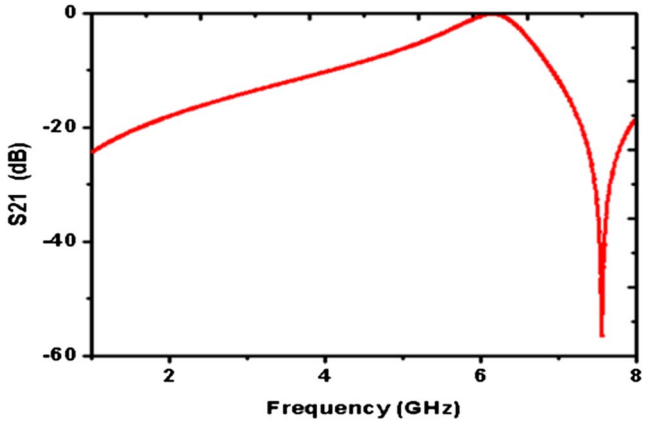


Figure 3. Response of the structure of Figure 2(a) and (b).

The bottom layer is used for the biasing arrangement. It is connected to the upper layer by four metallic vias of radius (R_1) = 0.5 mm to bias the varactor diode. The biasing arrangement uses the unit-cell's geometry and the lumped elements to bias the varactor diode. For this purpose, four inductances are used at the bottom layer to complete the DC biasing arrangement. The biasing arrangement enables the varactor diode to be reverse-biased when the DC voltage is applied to the structure. The design parameters of the unit-cell are given in Table 1. A simple design structure with a high tuning ratio has been developed. The 3D view of the structure of the unit-cell under the full wave simulation environment in the CST microwave studio is shown in Fig. 1(c).

Inherently, the square-loop has band-stop filtering characteristics. However, two concentric square loops in the unit-cell connected through the varactor diode result in the reconfigurable bandpass AFSS design. The unit-cell has a periodicity (P) of 20 mm. To start the design, a simple square-loop structure without tuning elements, as shown in Fig. 2, was simulated in the CST Microwave Studio. The response of the structure is shown in Fig. 3.

The structure exhibits a bandstop behavior in the 1–4 GHz band, where S_{21} is less than – 10 dB. Further, the transmission pole and zero appear at 6 and 7.5 GHz, respectively. It indicates that inherently, the topology has bandstop characteristics in the 1–4 GHz band. To make the structure reconfigurable and to accommodate active and biasing elements, slots have been cut in the stubs at the top and bottom layers, as shown in the structure. Further, as indicated in Fig. 4(a) and (b), four vias of $R_1 = 0.5$ mm are placed to provide the biasing voltage to the active element at the top layer. The response of these arrangements is shown in Fig. 5. From this figure, it is interpreted that the transmission pole shifts marginally from 6 to 5.5 GHz, but the transmission zero shifts significantly from 7.5 to 6.30 GHz.

In this scenario, the −3 dB bandstop response is 3.4 GHz. The effect of the change of radius of the metallic via's and the slot position has been parametrically varied, but no significant change has been observed. Figure 6 shows the structure's response when the radius of the vias is varied from 0.1 to 0.5 mm. In the structure, as shown for biasing the active elements, four inductors per unit-cell have been placed at the bottom layer in Fig. 2(b). The purpose of the inductor is only to pass the direct current without interfering with the RF signal. The value of the inductor is to be selected so that it does not change the unit-cell response.

An inductor of 15 nH each has been placed in the slots at the bottom layer to meet this requirement. It has been noticed that it does not influence the unit-cell response, as shown in Fig. 5. The structure has been simulated with different values of inductors. There is no significant change in the response, as shown in Fig. 7.

To achieve the reconfigurability in the L–S bands of the electromagnetic spectrum, the varactor diode SMV1430, represented by the series combination of resistance ($RR1$), inductance ($LL1$), and capacitance ($CC1$), where $RR1 = 3.15$ ohms, $LL1 = 0.45$ nH, and $CC1 = 1.24$ pF, is used in the structure. A total of 4 varactor diodes per unit-cell have been placed on the top layer, as shown in Fig. 2(a). When the diode is placed in the circuit, in the OFF state, the response is like the response to the previous case observed with the inductor. Further, to demonstrate that the structure exhibits a similar response to that of the unit-cell without a varactor diode. Finally, with the varactor diode, the structure is simulated. Its response is shown in Fig. 8. The result shows the proposed structure's frequency tuning capability when the varactor diode's capacitance

https://doi.org/10.1017/S1759078725102675 Published online by Cambridge University Press

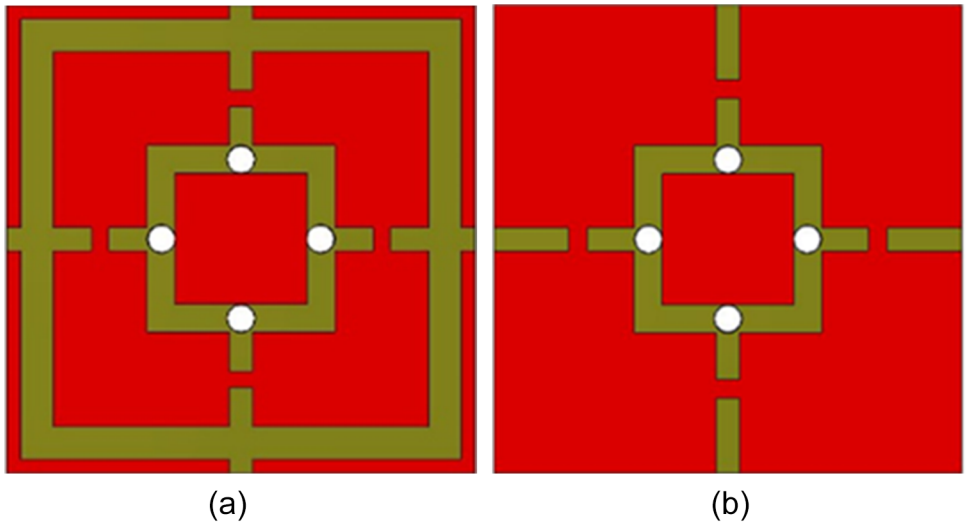


Figure 4. Unit-cell with vias (a) front, and (b) back view.

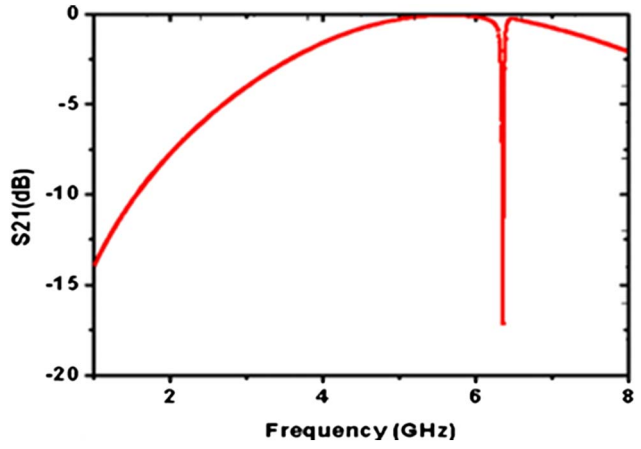


Figure 5. Response of the structure of Figure 4(a) and (b).

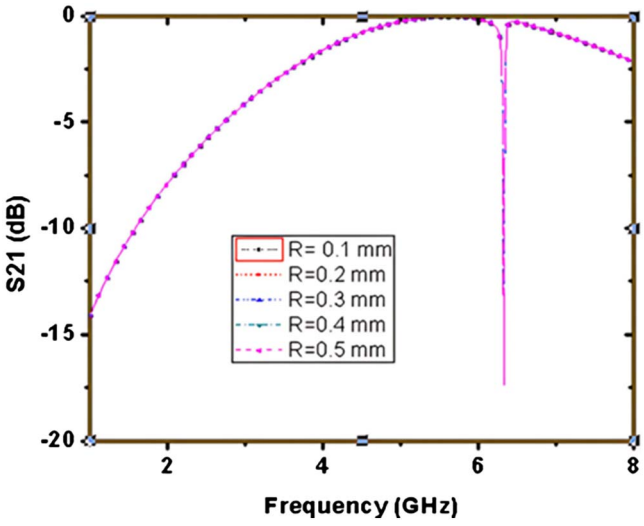


Figure 6. Response of the structure by varying the radius of the via's.

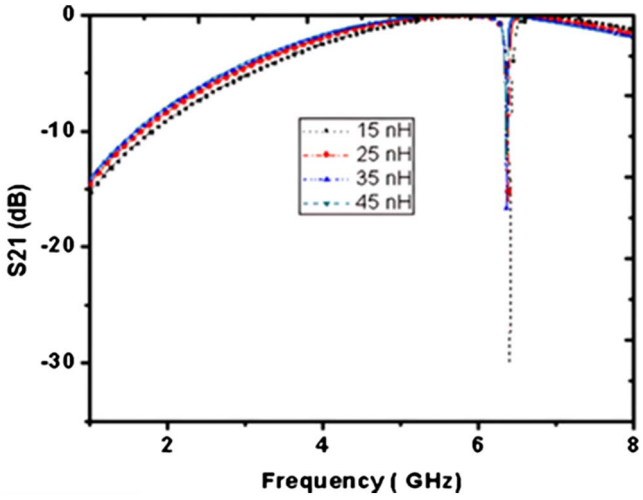


Figure 7. Response of the structure of varying inductors.

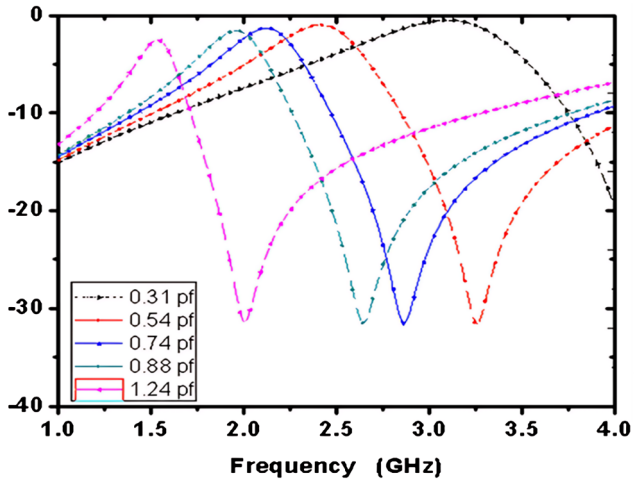


Figure 8. Response of the structure of varying capacitance.

https://doi.org/10.1017/S1759078725102675 Published online by Cambridge University Press

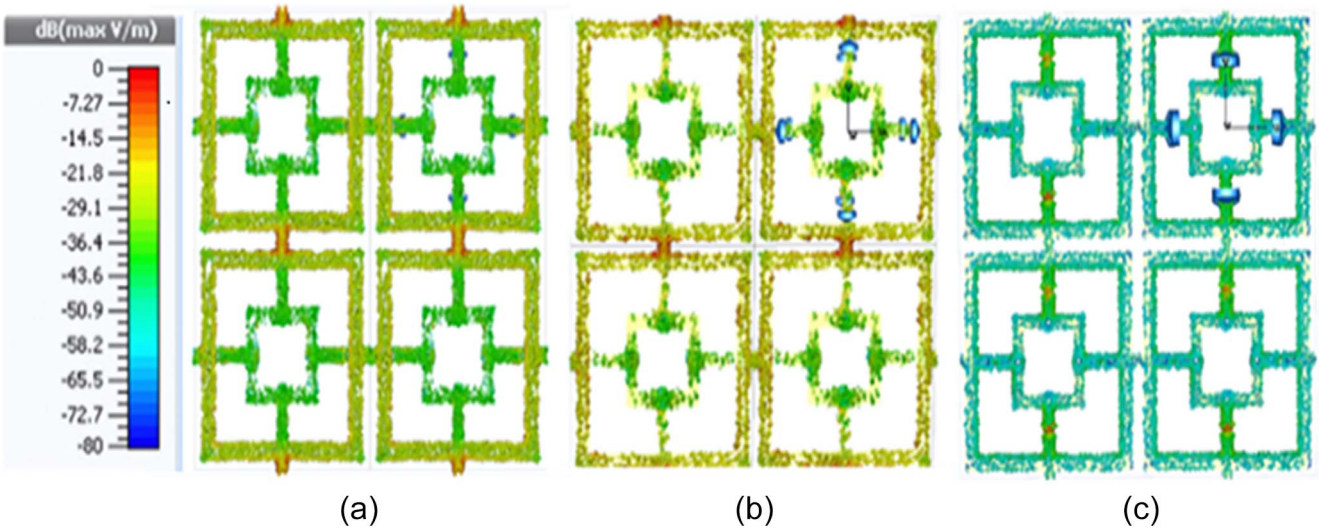


Figure 9. Surface current densities of the structure (a) without diode at 1.58 GHz, (b) with diode at 1.58 GHz, and (c) with diode at 3.1 GHz.

(CC1) varies from 1.24 to 0.31 pF, corresponding to 0 and 30 V, respectively.

These are the two extremes of the applied biasing voltages to this diode. For the three intermittent values of *CC*1, the unit-cell's response is also shown in Fig. 8. It is observed that the structure can be reconfigured from 1.53 to 3.1 GHz with a tuning bandwidth of 101.30%. The minimum −3 dB bandwidth of the 100 MHz band is achieved at the lowest operating band, corresponding to $CC = 1.24$ pF, and 800 MHz bandwidth, corresponding to $CC1 = 0.31$ pF.

Equivalent circuit model

For the physical insight into the working mechanism, the EC model is derived from the interpretation of the surface current density (J_S) on the unit cell. The J_S for different cases is shown in Fig. 9(a)–(c).

In Fig. 9(a), the inter unit-cell gap shows a discontinuity in the $J_{s,}$ thus having a capacitive (C_1) effect. The interconnecting stubs between unit cells have a stronger surface current, which indicates its inductive behavior. Thus, this inductor (L_1), in parallel to the gap capacitance (C_1), forms a parallel *L*–*C* circuit in the EC model, as shown in Fig. 10. The symmetric outer loop is modeled as an inductor (L_2). The inner square loop is modeled as (L_6). The inner square loop, along with the stub, represents another resonating circuit where inductance and capacitance have been modeled as L_2 and C_4, respectively. The back side of the structure has a square loop dominated by its inductive behavior, which is modeled by L_3 in Fig. 10. The metallic vias used to connect the upper and lower layers of the metallic strips also show the inductive behavior modeled by L_5.

To make the structure tunable, a varactor diode can be placed to connect the outer square loop to the inner square loop, which is modeled as a series RLC circuit represented by the combination of *RR*1, *LL*1, and *CC*1. The value of *CC*1 can be set to different values. In the case of 1.24 pF (0 V biasing voltage), the current density on the unit-cell surface is shown in Fig. 9(b). In this case, the stronger J_S on the outer loop can be observed but diminishes at the inner loop's corners, indicating the current flow through the diode and thus controlling the resonance frequency [34]. When *CC*1 is reduced to 0.31 pF, the J_S is further reduced, as shown in Fig. 9(c). In this case, due to the lower value of the CC1, the quality factor is reduced, and the bandwidth is increased, compared to the case when $CC1 = 1.24$ pF.

The ECM of the unit cell can be drawn using the inductors and capacitors. The lumped elements are characterized using the band of operation and the parasitic and other effects for the full-wave EM Simulations. The value of inductors can be calculated using the approximate design equation in which *L, W, t*, and kg are the length of the metallic segment, the width of the segment (in μm), the thickness of the segment, and the correction factor, respectively [35]. Here, *m* is an integer that represents the inductance number, as shown in Fig. 10. The correction factor is due to the use of the dielectric support on which the inductor has been formed. The value of the correction factor is 0.59 to include the effect of the ground plane:

$$L_m(\text{nH}) = 2 \times 10^{(-4)} \times l \left[\ln\left(\frac{l}{W+t}\right) + 1.193 + 0.2235\left(\frac{W+t}{l}\right)\right] \times \text{kg}. \quad (1)$$

The capacitance value between the sections in the EC model is a closed expression without dielectric material and is calculated using (2), where again, *m* is an integer representing the capacitance number in the EC model, as shown in Fig. 10 [36]. In this case, *L*, ε_0, ε_r' Furthermore, g_K is the length of the segment (in μm), the relative permittivity of free space, the real part of the relative permittivity of the substrate material used, and the inter-element gap distance, respectively:

$$C_m\,(p\text{F}) = (2L\varepsilon_0/\pi)\sin^{-1}(\pi g_k/2L). \quad (2)$$

However, when the dielectric material is considered, the capacitance relation gets modified as follows [36]:

$$C_d\,(p\text{F}) = (2l\varepsilon_0\varepsilon'_r/\pi)\sin^{-1}(\pi g_k/2l). \quad (3)$$

Based on these equations, the lumped parameters of the EC model have been retrieved and shown in Table 2. The two-port networks play a critical role in modeling RF and microwave systems, where frequency-dependent behavior and impedance matching are key design considerations.

Thus, here, the objective is to derive the ABCD parameters that comprehensively describe the electrical characteristics of the circuit, especially its resonance and high-frequency performance.

https://doi.org/10.1017/S1759078725102675 Published online by Cambridge University Press

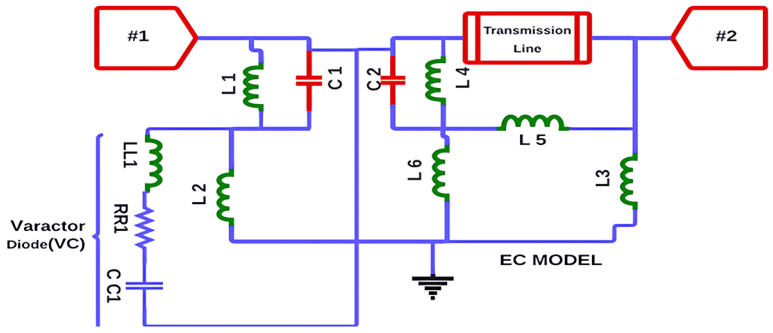


Figure 10. EC model of the structure.

Table 2. Design parameters of the unit-cell

Parameter	Value (mm)	Parameter	Value (mm)
L_1	15.34 nH	L_5	0.01 nH
L_2	7.67 nH	L_6	53.53 nH
L_3	7.67 nH	C_1	0.1 pF
L_4	20 nH	C_2	0.01 pF

The analyzed network comprises interconnected reactive components and a transmission line, forming a two-port symmetric structure. Here, the model comprises the following network element combinations:

i. Parallel LC Circuit (L_1 (Inductor) and C_1 (Capacitor) at Port 1.
ii. Series Inductor (L_2) grounded, influencing impedance.
iii. Varactor diode (RR_1, LL_1, CC_1) providing tunable resonance.
iv. Parallel LC circuit L_4 (inductor) and C_2 (capacitor). Connected via a transmission line.
v. Delta network (L_3 L_5 L_6) at Port 2, where

- L_6 and L_3 are grounded.
- L_5 L_6 are connected to $L_4 \parallel C_2$.
- L_3 L_5 are connected to Port 2.

Outer loop: A parallel combination of L_1 (inductor) and C_1 (capacitor). Inner loop: A more complex structure comprising a parallel combination of C_2 (capacitor) and L_4 (inductor), delta configuration of three inductors: L_3, and .

Transmission line: Connecting the inner loop to the backside loop.

The admittance of the parallel combination of L_1 and C_1 with the impedance of a series inductor L_2 Impedance of varactor diode $CC1$ (for a case $CC1$ and parallel circuit and C_2) are calculated as $=j\omega C_1+= j\omega L_2$, $Z_{CC}= RR_1+LL_1+1j\omega CC_1$, $Y_D =j\omega C_2+1/j\omega L_4$.

The delta configuration is converted into a Y (star) configuration with admittances.

Y_{L_3}, Y_{L_5}& $Y_{L_6}, Y_{L_3} = \frac{L_3 L_6}{L_3+L_5+L_6}, Y_{L_5} = \frac{L_3 L_5}{L_3+L_5+L_6} Y_{L_6} = \frac{L_5 L_6}{L_3+L_5+L_6}$, respectively.

The ABCD parameters are calculated as

$$ABCD_A = \begin{bmatrix} 1 & 0 \\ Y_A & 1 \end{bmatrix}, \quad (4)$$

$$ABCD_B = \begin{bmatrix} 1 & Z_B \\ 0 & 1 \end{bmatrix}, \quad (5)$$

$$ABCD_{CC} = \begin{bmatrix} 1 & Z_{CC} \\ 0 & 1 \end{bmatrix}, \quad (6)$$

$$ABCD_D = \begin{bmatrix} 1 & 0 \\ Y_D & 1 \end{bmatrix}, \quad (7)$$

$$ABCD_{Y_{L6}} = \begin{bmatrix} 1 & j\omega Y_{L_6} \\ 0 & 1 \end{bmatrix}, \quad (8)$$

$$ABCD_{Y_{L_3}} = \begin{bmatrix} 1 & j\omega Y_{L_3} \\ 0 & 1 \end{bmatrix}, \quad (9)$$

$$ABCD_{Y_{L_5}} = \begin{bmatrix} 1 & 0 \\ \frac{1}{j\omega Y_{L_5}} & 1 \end{bmatrix}. \quad (10)$$

The cascaded $ABCD$ matrix for the network is $ABCD_{Total}$:

$$ABCD_{Total} = ABCD_A \times ABCD_B \times ABCD_{CC} \times ABCD_D \times ABCD_{Y_{L_6}} \times ABCD_{Y_{L_3}} \times ABCD_{Y_{L_5}} \quad (11)$$

This results in the calculation of the ABCD parameters, which are as follows:

$$A = 1 + j\omega Y_{L_6} Y_D + j\omega Y_{L_3} Y_D, \quad (12)$$

$$B = j\omega Y_{L_3} + j\omega Y_{L_5} + j\omega Y_{L_6} + Z_{CC} \quad (13)$$

$$C = Y_A + Y_B + Y_D + \frac{1}{j\omega Y_{L_5}} \quad (14)$$

$$D = 1 + j\omega Y_D Y_{L_5}. \quad (15)$$

Thus, using the conversion formula from ABCD to S-parameters, we can deduce the $S_{11}, S_{22}, S_{21}, S_{12}$. The circuit exhibits reciprocity, ensuring that the transmission properties of the circuit are correct.

Theoretical validation

To validate the concept and accuracy of the retrieved lumped parameters of the unit cell as shown in Table 2, the reconfigurable response of the unit cell is shown in Fig. 11. The comparison of the result of the unit-cell simulation in the CST Microwave Studio and

https://doi.org/10.1017/S1759078725102675 Published online by Cambridge University Press

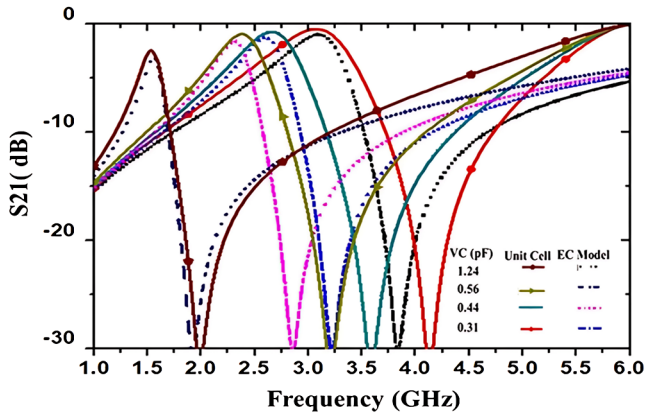


Figure 11. Comparison of unit cell and EC model responses.

the analytically obtained value of the responses are shown here for the different values of the varactor capacitances. The analytical and simulated results agree to reveal the accuracy of the EC model of a tunable FSS, which has seldom been investigated in the literature.

It is clear from the simulation results that the proposed AFSS and the EC model can reconfigure the frequency between 1.53 and 3.1 GHz band for different values of the varactor diode's capacitance range of 1.24 to 0.31 pF. These capacitances correspond to the two extremes, i.e., 0 and 30 V, which are applied biasing voltages to the SMV1430 [37].

Fabrication and experimental results

The AFSS was fabricated using the traditional wet etching of the planar circuit board (PCB), and the pattern was created using screen printing on both sides of the copper-cladded Rogers RT5880 substrate material. Once the PCB was fabricated, vias were manually drilled and connected via metallic wires with a radius of 0.5 mm. The AFSS structure of 10 × 10 unit-cells (20 cm × 20 cm) was prototyped as shown in Fig. 12. The biasing arrangement of the AFSS structure is shown in Fig. 13(a)–(c). The front view of the AFSS structure in which it is shown that all the outer square loops are interconnected to each other, on which the positive terminal of the supply voltage is connected. Thus, at any given point, the supply voltage is made available to all the outer loops of the unit-cells. Since the cathode of all the varactor diodes is connected to the outer loop, the positive supply voltage is made available to the cathode of all the varactor diodes in each unit-cell of the AFSS structure. It is evident from Fig. 13(a) that all the diodes in a unit cell are connected in parallel. Thus, this simple biasing technique activates all the diodes in a unit cell.

The biasing arrangement of the back side of the AFSS structure is shown in Fig. 13(b). In this figure, all the backside square loops are connected through the inductors placed in each stub. It is pertinent that the size of the bottom square loop is the same as the size of the inner square loop at the front face of the unit-cell. These loops are connected through the four no's of metallic vias per unit-cell. The negative supply is made available through the arrangement at the inner loop of the front face of the AFSS. The schematic diagram of the interconnect of the via is shown in Fig. 13(c). Since the anode of the varactor diode is connected to the inner loop. Thus, the negative supply is available for the varactor diode. Therefore, a reverse biasing potential is available across each varactor diode for reconfiguration.

The response of the structure was measured in the Antenna and Microwave Design Laboratory, Shri Mata Vaishno Devi University, India, using a bistatic measurement setup, as shown in Fig. 12(c). The experimental arrangement comprised two pairs of horn antennas operating between 1–2 and 2–4 GHz, respectively. Furthermore, considering the antennas' maximum dimension (M), the far-field distance of these antennas at their maximum operating frequency is calculated using the formula $2 \times M^2/\lambda$.

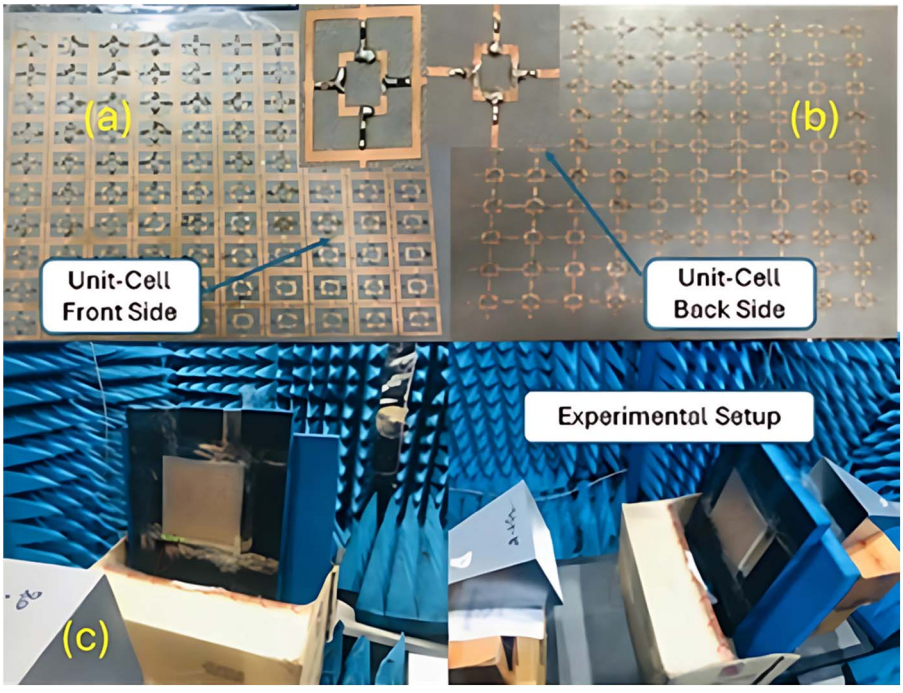


Figure 12. Fabricated structure front and back, with experimental setup.

https://doi.org/10.1017/S1759078725102675 Published online by Cambridge University Press

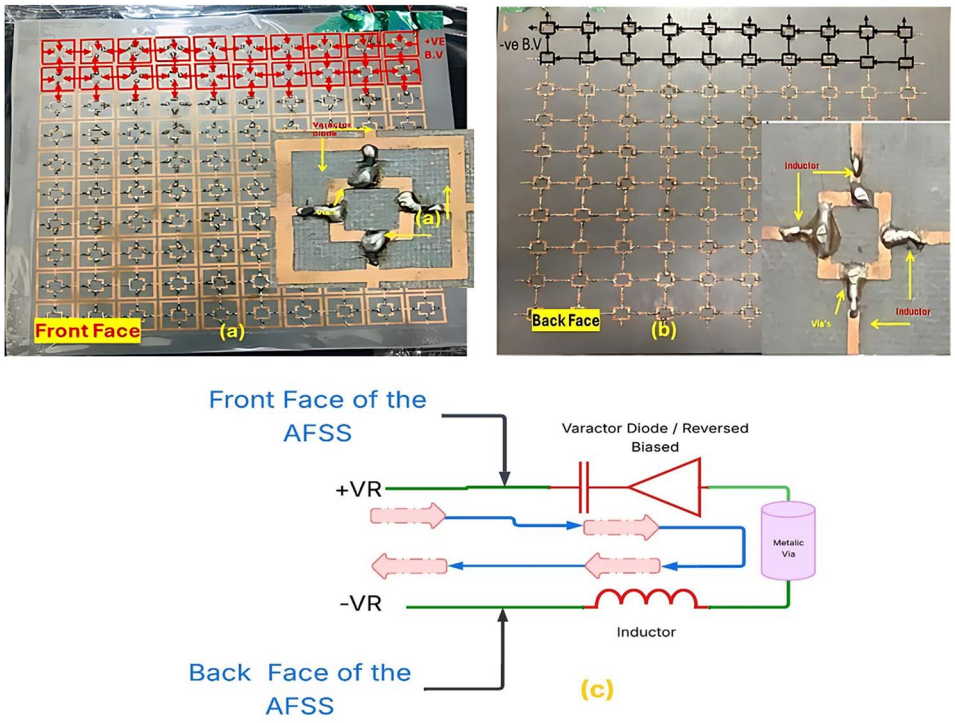


Figure 13. Biasing arrangement (a) front face, (b) back face, and (c) schematic diagram.

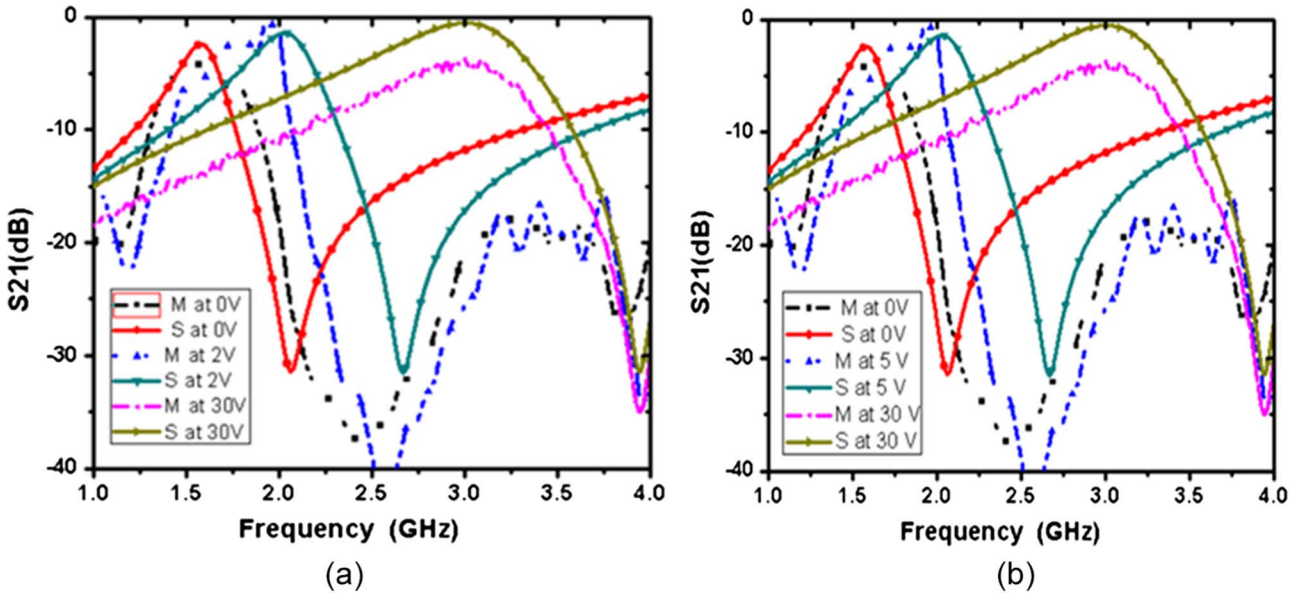


Figure 14. Simulated and measured response for AOI = 0° (a) TE, (b) TM mode.

The maximum aperture width of the horn antenna used in the measurement was $M = 23.5$ cm, and thus, for the far-field criteria measurement, the horn was placed at a distance of 1.5 m away from the AFSS. The power supply voltage was varied from 0 to 30 V, and the responses of the structure for the various angles of incidence are shown in Figs. 14–17.

Measurement at normal incidence

The structure was measured for the normal and angular incidence of the incident wave on it. The measurement was done by first measuring the transmission coefficient in the free Space (S_{21}) (without structure) for reference, and then, the transmission coefficient of the prototype was measured. The response of the structure for the normal incidence of the electromagnetic (EM) wave in the transverse electric (TE) and transverse magnetic (TM) modes is shown in Fig. 14(a) and (b), respectively. In the TE mode, the FSS has a 1.58–3.0 GHz simulated and 1.53–3.1 GHz measured tunable frequency range. Similarly, from Fig. 14(b), it is revealed that the simulated and the measured tuning ranges for TM mode are 1.57–3.0 and 1.56–2.70 GHz, respectively. For the TE mode, the simulated and measured frequency tuning range is in good

https://doi.org/10.1017/S1759078725102675 Published online by Cambridge University Press

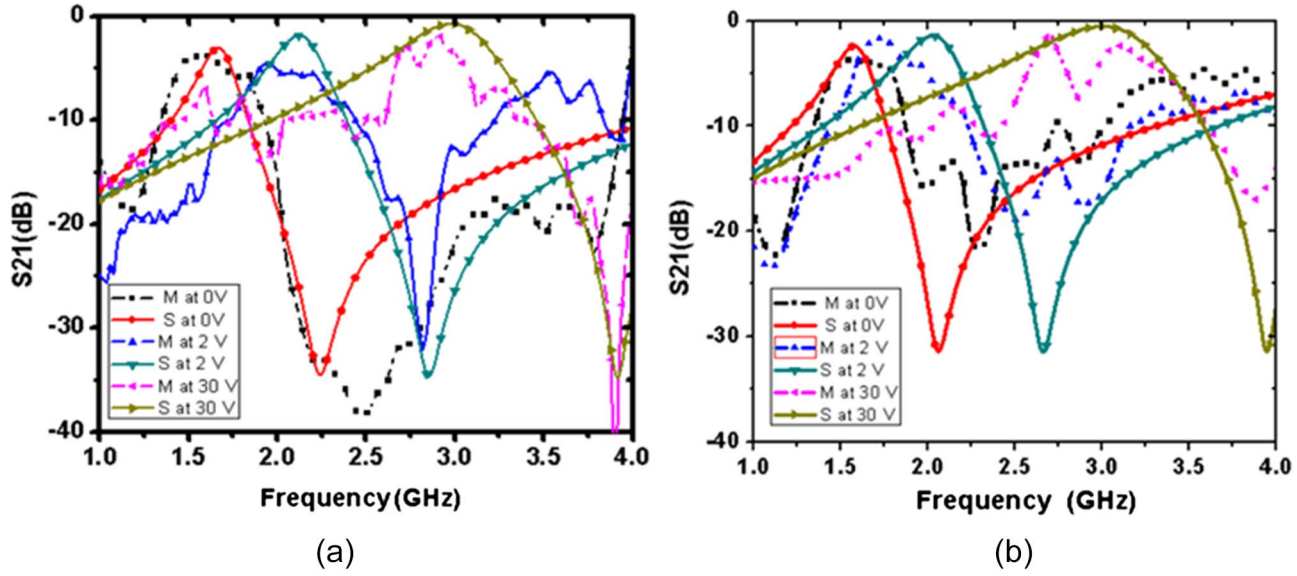


Figure 15. Simulated and measured response for AOI = 15° (a) TE and (b) TM mode.

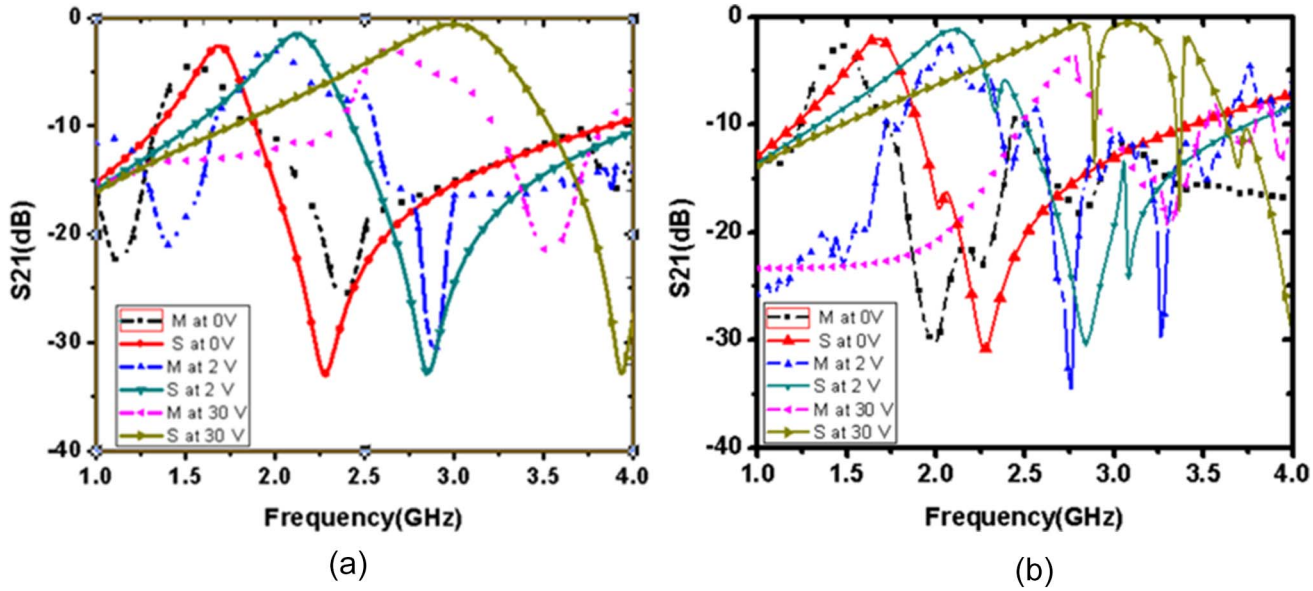


Figure 16. Simulated and measured response for AOI = 30° (a) TE and (b) TM mode.

agreement. However, the maximum operating frequency for the TM mode has been reduced to 2.70 GHz. This is mainly due to the tolerances associated with the fabrication process, the effect of handheld soldering in the laboratory, and the characteristic variation of the individual varactor diode. The tuning ratio is defined as the fou/fol, where fou and fol are the resonant frequencies of the upper and lower tuned bands, as shown in Table 3.

Angular incidence

In addition to the normal incidence, the structure has also been tested for the angular incidences of 15°, 30°, and 45°. The responses of the structure for the AOI = 15°, AOI = 30°, and AOI = 45° for TE and TM modes are in Figs. 15, 16, and 17, respectively.

It is evident from these figures that with the increase in the angle of incidence, the insertion loss increases and the operating band shrinks. This is mainly due to the fabrication tolerance and the change in the characteristic impedance of TE and TM modes with a change in the angle of incidence. It is expected that by enhancing the fabrication facility, fabrication tolerances can be minimized.

However, with conciseness, we have demonstrated the dual-polarized response of the reconfigurable FSS structure up to the 45° angle of incidence. For the comparison, the other performance indices of the proposed tunable FSS are placed in Table 3.

State-of-the-art comparison

To ascertain the contribution of the proposed reconfigurable FSS, it has been compared to the existing structures, and the state-of-the-art comparison is shown in Table 4. This table shows that the proposed FSS has a wider tuning ratio than others, except for the structure presented in [31]. However, it is at the cost of

https://doi.org/10.1017/S1759078725102675 Published online by Cambridge University Press

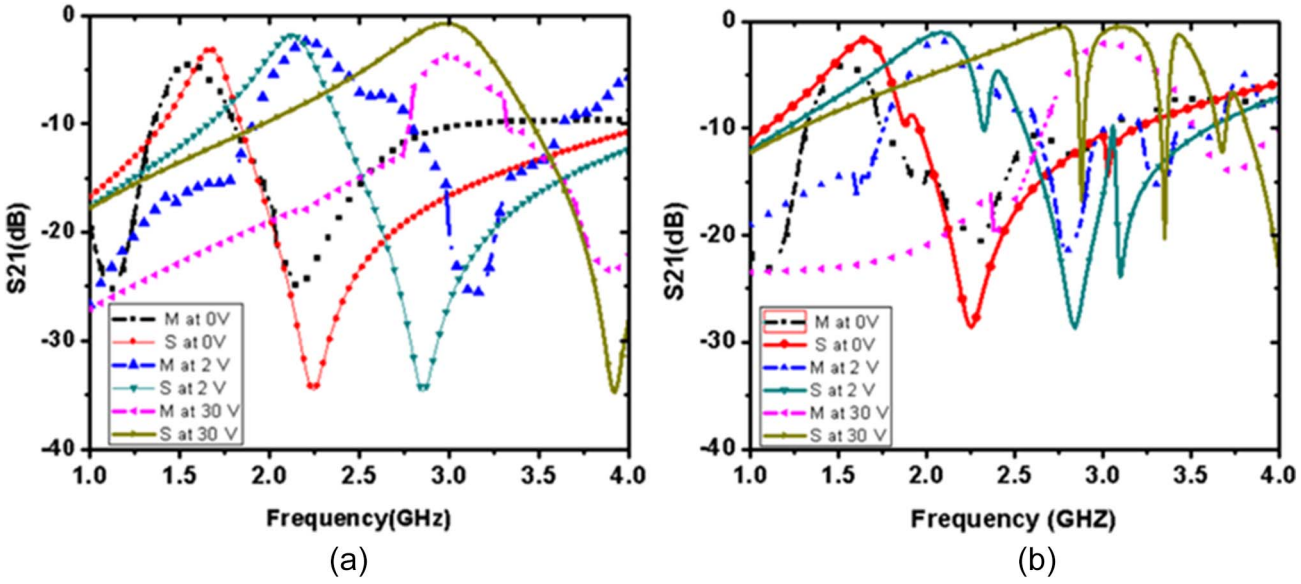


Figure 17. Simulated and measured response for AOI = 45° (a) TE and (b) TM mode.

Table 3. Comparison of angular performances

TE MODE						
	Simulated		Measured		F_{ou}/f_{ol} ratio	
AOI (Degree)	TR (GHz)	IL (dB)	TR (GHz)	IL (dB)	Sim.	Meas.
0	1.58–3.0	0.51–2.37	1.53–3.1	3.73–3.82	1.89	2.02
15	1.68–2.90	1.71–3.72	1.58–2.90	0.70–3.05	1.77	1.83
30	1.68–2.99	0.58–2.58	1.54–2.64	2.98–4.42	1.77	1.71
45	1.66–2.98	0.70–3.05	1.54–3.0	3.69–4.43	1.79	1.94
TE MODE						
	Simulated		Measured		F_{ou}/f_{ol} ratio	
AOI (Degree)	TR (GHz)	IL (dB)	TR (GHz)	IL (dB)	Sim.	Meas.
0	1.57–3.0	1.16–3.63	1.56–2.70	0.50–2.37	1.91	1.73
15	1.57–3.0	0.50–2.37	1.58–2.70	1.16–3.63	1.91	1.73
30	1.67–3.09	0.507–2.03	1.46–2.78	2.21–3.31	1.85	1.9
45	1.68–2.78	0.483–1.70	1.50–3.04	2.00–4.10	1.65	2.02

Table 4. State-of-the-art comparison of reconfigurable FSS

Ref.	Non-linear element	Tuning range (GHz)	Unit cell (λ_L^2)	Angular stability up to (degree)	Polarization insensitive	Tuning ratio	Insertion loss (dB)	No. of dielectric layers
[17]	Varactor & P-I-N	3.70–4.27	0.123 × 0.123	45	Yes	1.15	1.96–4.27	Single
[21]	Varactor	3.70–5.20	0.098 × 0.098	60	Yes	1.40	3–6	Double
[30]	Varactor	3.62–4.25	0.12 × 0.12	45	Yes	1.17	0.72–1.10	Single
[31][a]	Varactor & P-I-N	1.51–3.84	0.50 × 0.50	70	No	2.54	0.35–2.55	Single
[32]	Varactor	4.92–5.84	0.01 × 0.01	45	No	1.18	0.51–1.09	Single
[33]	P-I-N	2.57–2.61	0.51 × 0.51	45	Yes	1.01	0.03	Single
Proposed	**Varactor**	**1.53– 3.10**	**0.10 × 0.10**	**45**	**Yes**	**2.02**	**1.1–3.82**	**Single**

[a]On state of PIN diode.

https://doi.org/10.1017/S1759078725102675 Published online by Cambridge University Press

circuit complexity as varactor and PIN diodes have been used simultaneously in [31]. In addition, the structure proposed in [31] is polarization-sensitive, limiting its applications. Most of the dual-polarized structures have been measured for angular insensitivity up to 45° except the structure reported in [21]. However, that structure uses double dielectric layers, resulting in a high insertion loss. In view of this comparison, it is concluded that the proposed structure in this manuscript offers a high tuning ratio, with reasonably low insertion loss and polarization insensitivity up to 45°. The structure may find its applications in stealth technology and beam steering of the antennas for the ISM and sub-6 GHz band applications.

Conclusion

This paper proposes a simple dual-polarized AFSS with angular stability up to 45°. Using varactor diodes, it has been demonstrated that the AFSS can be reconfigured over the 1.53–3.10 GHz frequency band, offering a high tuning ratio of 2.02. The proposed unit-cell has been rigorously analyzed to retrieve the network parameters of the EC Model for different reconfigurable states. Due to the dual-polarized reconfigurable response, in addition to the conventional use in the radome and the stealth technology, newser applications may be found in the beam steering of the antennas. Since the structure has stable angular responses, it may also be used in tilted-beam-steered antenna design in the future.

Author contributions. Ashish Suri conceptualized and interpreted the findings of the various papers and wrote the manuscript draft. Kumud R. Jha supervised, reviewed, and helped arrive at the manuscript's conclusion.

Funding statement. This research received no specific grant from any funding agency, commercial or not-for-profit sectors.

Competing interests. The authors report no conflict of interest.

References

1. **Munk BA** (2000) *Frequency Selective Surfaces: Theory and Design*. New York, NY, USA: Wiley.
2. **Wu TK** (1995) *Frequency Selective Surface and Grid Array*. New York, NY, USA: Wiley.
3. **Li M and Shen Z** (2023) Low-RCS transmit array based on 2.5-D cross-polarization converter. *IEEE Transactions on Antennas and Propagation* **71**, 5828–5837. https://doi.org/10.1109/TAP.2023.3271149
4. **Bakshi SC, Mitra D and Teixeira FL** (2021) Multifunctional frequency selective rasorber with dual mode and continuous tunability. *IEEE Transactions on Antennas and Propagation* **69**, 5704–5715. https://doi.org/10.1109/TAP.2021.3061127
5. **Zhao Y, Fu J, Wang Z, Chen W, Lv B and Zhang Q** (2022) Broadband switchable active frequency selective surfaces based on modified diode model. *IEEE Antennas and Wireless Propagation Letters* **21**, 1378–1382. https://doi.org/10.1109/LAWP.2022.3168983
6. **Li H, Costa F, Fang J, Liu L, Wang Y, Cao Q and Monorchio A** (2019) Miniaturized multifunctional active frequency-selective surface. *IEEE Transactions on Antennas and Propagation* **67**, 4659–4667. https://doi.org/10.1109/TAP.2019.2911271
7. **Vilas Boas EC, Filgueiras HRD, Feliciano da Costa I, Ribeiro JAJ and Sodre AC** (2019) Dual-band switched-beam antenna array for MIMO systems. *IET Microwaves, Antennas & Propagation* **14**, 82–87. https://doi.org/10.1049/iet-map.2019.0010
8. **Wen JM, Wang CK, Hong W, Pan YM and Zheng SY** (2021) A wideband switched-beam antenna array fed by a compact single-layer Butler matrix. *IEEE Transactions on Antennas and Propagation* **69**, 5130–5135. https://doi.org/10.1109/TAP.2021.3060040
9. **Naseri H, Pourmohammadi P, Fei P, Melouki N, Iqbal A and Denidni T** (2023) Butler matrix-based beamforming with polarization reconfigurability for reducing electromagnetic interference. *AEU - International Journal of Electronics and Communications* **170**, 154833. https://doi.org/10.1016/j.aeue.2023.154833.
10. **Bora P, Pardhasaradhi P and Madhav B** (2020) Design and analysis of EBG antenna for Wi-Fi, LTE, and WLAN applications. *The Applied Computational Electromagnetics Society Journal (ACES)* **35**, 1030–1036. https://doi.org/10.47037/2020.ACES.J.350908
11. **Alhaj Hasan A, Nguyen TM, Kuksenko SP and Gazizov TR** (2023) Wire-grid and sparse MoM antennas: Past evolution, present implementation, and future possibilities. *Symmetry* **15**, 378–378. https://doi.org/10.3390/sym15020378
12. **Zhang L-M, Ding X and Shao W** (2021) A phase compensation beam switching antenna based on frequency selective surface. *IEEE Antennas and Wireless Propagation Letters* **20**, 1741–1744. https://doi.org/10.1109/LAWP.2021.3095366
13. **Ali H** (2024) Spherical active frequency-selective surface for 3-D beam-scanning antenna. In *2024 18th European Conference on Antennas and Propagation (EuCAP)*, pp. 1–4. Glasgow, United Kingdom. https://doi.org/10.23919/EuCAP60739.2024.10501484
14. **Elzwawi GH, Kesavan A, Alwahishi R and Denidni TA** (2020) A new corner-reflector antenna with tunable gain based on active frequency selective surfaces. *IEEE Open Journal of Antennas and Propagation* **1**, 88–94. https://doi.org/10.1109/OJAP.2020.2979053
15. **Rai JK, Ranjan P and Chowdhury R** (2024) Recent development in reconfigurable dielectric resonator antenna and microwave filter: Design and application. *International Journal of Communication Systems* **37**(14). https://doi.org/10.1002/dac.5859
16. **Qasem NE and Alamayreh A** (2022) Dual-band millimeter-wave beam scanning slotted square patch antenna based on active frequency selective surfaces for 5G applications. *International Journal on Communications Antenna and Propagation (IRECAP)* **12**, 30. https://doi.org/10.15866/irecap.v12i1.21574
17. **Kong D, Li H, Luo Q and Gao S** (2020) Electronically beam-scanning antenna with active slot frequency selective surface for 5G base stations. in *2020 IEEE MTT-S International Wireless Symposium (IWS)*, Shanghai, China, pp. 1–3. https://doi.org/10.1109/IWS49314.2020.9360164
18. **Phon R, Ghosh S and Lim S** (2019) Active frequency selective surface to switch between absorption and transmission band with additional frequency tuning capability. *IEEE Transactions on Antennas and Propagation* **67**, 6059–6067. https://doi.org/10.1109/TAP.2019.2916752
19. **Borhani-Kakhki M and Denidni TA** (2023) Metamaterial enabled FSS for beam-tilting mm-wave antenna applications in Choudhury, B. and Tewary, V. K. (eds.), *Handbook of Metamaterial-derived Frequency Selective Surfaces*, Vol. 3. Singapore: Springer Nature, pp. 453–474.
20. **Ahmed F, Singh K and Esselle KP** (2023) State-of-the-art passive beam-steering antenna technologies: Challenges and capabilities. *IEEE Access* **11**, 69101–69116. https://doi.org/10.1109/ACCESS.2023.3278570
21. **Carreira P** (2019) Electronically reconfigurable FSS – inspired transmitarray for two dimensional beamsteering for 5G and radar applications at 28 Ghz. Doctoral dissertation.
22. **Ebrahimi A, Shen Z, Withayachumnankul W, Al-Sarawi SF and Abbott D** (2016) Varactor-tunable second-order bandpass frequency-selective surface with embedded bias network. *IEEE Transactions on Antennas and Propagation* **64**, 1672–1680. https://doi.org/10.1109/TAP.2016.2537378
23. **Ali Q, Shahzad W, Ahmad I, Safiq S, Bin X, Abbas SM and Sun H** (2022) Recent developments and challenges on beam steering characteristics of reconfigurable transmitarray antennas. *Electronics* **11**, 587–587. https://doi.org/10.3390/electronics11040587
24. **Sathuluri MR and Sasikala G** (2020) Reconfigurable antenna using RF MEMS switches issues and challenges: A survey. *Advances in Intelligent Systems and Computing* **1163**, 119–134.
25. **Isa SR, Jusoh M, Sabapathy T, Nebhen J, Kamarudin MR, Osman MN, Abbasi QH, Rahim HA and Yasin MN** (2021) Reconfigurable pattern patch antenna for mid-band 5G: A review. *Computers, Materials & continua/Computers, Materials & Continua (Print)* **70**(2), 2699–2725.

https://doi.org/10.1017/S1759078725102675 Published online by Cambridge University Press

26. **Panwar R and Lee JR** (2017) Progress in frequency selective surface-based smart electromagnetic structures: A critical review. *Aerospace Science and Technology* **66**, 216–234.
27. **Beneck RJ, Das A, Mackertich-Sengerdy G, Chaky RJ, Wu Y, Soltani S and Werner D** (2021) Reconfigurable antennas: A review of recent progress and prospects for the next generation. *Progress In Electromagnetics Research* **171**, 89–121.
28. **Alwareth H, Ibrahim IM, Zakaria Z, Al-Gburi AJA, Ahmed S and Nasser ZA** (2022) A wideband high-gain microstrip array antenna integrated with frequency-selective surface for sub-6 GHz 5G applications. *Micromachines* **13**, 1215. https://doi.org/10.3390/mi13081215
29. **Gong S, Lu X, Hoang DT, Niyato D, Shu L, Kim DI and Liang YC** (2020) Towards smart wireless communications via intelligent reflecting surfaces: a contemporary survey. *IEEE Communications Surveys & Tutorials* **22**, 2283–2314.
30. **Anand Y and Mittal A** (2020) Tuneable frequency selective surface. *Progress In Electromagnetics Research C* **101**, 13–28. https://doi.org/10.2528/PIERC19123104.
31. **Bai H, Yan M, Li W, Wang J, Zheng L, Wang H and Qu S** (2021) Tunable frequency selective surface with angular stability. *IEEE Antennas and Wireless Propagation Letters* **20**, 1108–1112. https://doi.org/10.1109/LAWP.2021.3073907
32. **Yang C, Li H, Cao Q and Wang Y** (2016) A dual-polarized switchable active frequency selective surface for LTE-D band. *Progress in Electromagnetics Research M* **48**, 77–85. https://doi.org/10.2528/PIERM16012003.
33. **Zhang L-M, Ding X and Bozzi M** (2024) Passband tunable reconfigurable frequency-selective surface with wide tuning range. *IEEE Transactions on Microwave Theory & Techniques* **72**, 5167–5178. https://doi.org/10.1109/TMTT.2024.3378979
34. **Guo M, Zheng Y, Chen Q, Ding L, Sang D, Yuan F, Guo T and Fu Y** (2021) Analysis and design of a high-transmittance performance for varactor-tunable frequency-selective surface. *IEEE Transactions on Antennas and Propagation* **69**, 4623–4632. https://doi.org/10.1109/TAP.2020.3045517
35. **Ganie JA, Jha KR and Sharma SK** (2022) Sub-1 GHz and sub-6 GHz reconfigurable MIMO antenna with 28 GHz array on shared chassis for user equipment's (UEs). *Journal of Electromagnetic Waves and Applications* **36**, 2473–2482. https://doi.org/10.1080/09205071.2022.2089916
36. **Hong J-SG and Lancaster MJ**. (2001) *Microstrip Filters for RF*. New York, etc: Wiley.
37. **Jha KR, Mishra G and Sharma SK** (2017) Design of a compact microwave absorber using parameter retrieval method for wireless communication applications. *IET Microwaves Antennas & Propagation* **12**, 977–985. https://doi.org/10.1049/iet-map.2017.0785
38. SMV1405-SMV1430 Series by Skyworks Solutions Inc. Datasheet | DigiKey (2021) Digikey.com.



Ashish Suri (MS, IEEE, M-ISTE, M-IE) received the Bachelor's degree in Electronics Engineering from the University of Pune, Maharashtra, India, in 2001; the Master's degree in Electronics and Communication Engineering from Punjab Technical University, India, in 2011; and is currently pursuing PhD degree in Electronics and Communication Engineering from Shri Mata Vaishno Devi University, Katra, UT of J&K, India. In 2001, he joined Model Institute of Engineering & Technology as a Lecturer and was promoted to Assistant Professor in 2007. In 2008, he joined Shri Mata Vaishno Devi University as an Assistant Professor. His current research includes microwave active component design for future wireless applications.



Kumud Ranjan Jha (IEEE M'17–SM'18, FIE (I)) received the Bachelor's degree in Electronics and Communication Engineering from The Institution of Engineers (India), Kolkata, India, in 1999; the Master's degree in Electronics and Communication Engineering from the Birla Institute of Technology, Ranchi, India, in 2007; and the PhD degree in Electronics and Communication Engineering from the Jaypee University of Information Technology, Waknaghat, India, in 2012. From September 2013 to September 2014, he was a Postdoctoral Fellow with the Department of Electrical and Computer Engineering at San Diego State University, San Diego, CA, USA. Before joining academia, he also served in the Indian Air Force for over one and a half decades. In 2007, he joined Shri Mata Vaishno Devi University, Katra, India, as an Assistant Professor and has been a Full Professor since 2020. He is the co-inventor of an Indian patent (published). He has authored/co-authored more than 90 research articles in journals and conferences. He has also co-authored the book Terahertz Planar Antennas for Next Generation Communication. He is credited with the book chapters in Multifunctional Antennas and Arrays for Wireless Communication Systems (IEEE Press/Wiley, USA, 2021). His current research interests include microwave/RF passive/active component design and terahertz electronics for future wireless applications.Dr. Jha is the recipient of the 2012 Raman Fellowship Award from the University Grant Commission, Government of India, for postdoctoral study in the USA. He is a Fellow of the Institution of Engineers (India). Dr. Jha is also a recipient of International Travel Grants from the Govt. of India to participate in IEEE Antenna Propagation Society Symposiums.

https://doi.org/10.1017/S1759078725102675 Published online by Cambridge University Press